FAILURE MODES OF CIRCULAR TUNNELS IN A TRANSVERSELY ISOTROPIC ROCK MASS

Van-Binh Bui [1], Yong-Ming Tien [2*], Charng Hsein Juang [3], and Yu-Chen Lu [4]

ABSTRACT

The stress concentration is one of the major causes of failure around the tunnel in a transversely isotropic rock mass. Knowledge about the features of damage helps tunnel engineers develop suitable countermeasures. In this paper, failure modes around the tunnel are studied through numerical analyses using the three-dimensional (3D) particle flow code (PFC3D). The transversely isotropic rock masses are generated with seven joint dip angles of 0°, 15°, 30°, 45°, 60°, 75°, and 90°. The tunnel excavation is simulated in 3D to study the effect of tunneling direction relative to the joint orientation on the tunnel stability. Various scenarios involving the tunneling direction, the joint strike, and joint dip are considered. Concerning the displacement around the tunnel, the displacement field (DF) may be grouped into one of the following four types: the tensile displacement field (DF-I and DF-II), the shear and tensile displacement field (DF-III), and the shear displacement along the joint (DF-IV). The failure mode may be described with one of the following five terms: (1) Detaching and Buckling, (2) Sliding, (3) Bending and Spalling, (4) Slabbing and Spalling, and (5) Falling. The failure modes at the crown, the sidewalls, and the invert of the tunnel in Scenarios 2 and 3 are similar. However, the failure modes in the tunnel face are different; the "Falling" mode is observed in Scenario 2, while the "Sliding" model is a risk in Scenario 3.

Key words: Failure modes, tunnel stability, tunneling direction, joint orientation, discrete element method, anisotropic rock mass.

1. INTRODUCTION

The anisotropic behavior is the fundamental characteristic of the transversely isotropic rock mass, in which the deformation and strength properties depend on the orientation of the bedding plane or joints. Excavation in a transversely isotropic rock mass for tunnel construction poses a significant challenge due to its anisotropic behavior. Tunneling direction relative to the orientation of bedding planes or joints has an essential impact on tunnel stability. In this study, the effect of tunneling direction with respect to the joint orientation on the failure modes around the tunnel is investigated. Three scenarios regarding the tunneling direction are considered. In Scenario 1, the tunneling direction is parallel to the joint strike. In Scenario 2, the tunneling direction is perpendicular to the joint strike with joints dipping along the tunneling direction (referred to as "tunneling with dip"). In Scenario 3, the tunneling direction is perpendicular to joint strike with joints dipping opposite to the tunneling direction (referred to as "tunneling against dip"). The three scenarios are shown in Fig. 1.

The observations from past tunnel projects showed that when the tunnel was driven parallel to the strike of bedding planes or joints, the failure of thin horizontal layers at the tunnel's
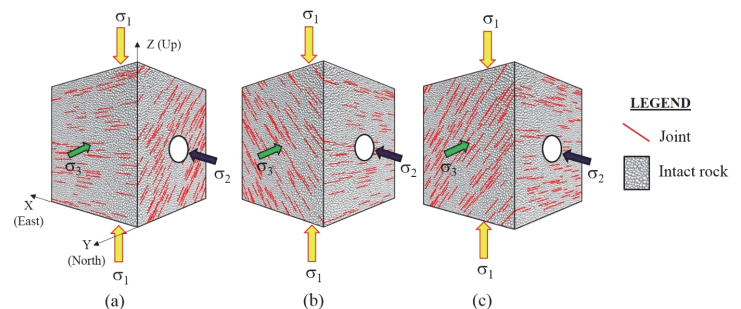

Fig. 1 Modeling tunnel excavation with different tunneling directions: (a) Scenario 1 - Tunnel axis parallel to joint strike; (b) Scenario 2 - Tunneling with dip; and (c) Scenario 3 - Tunneling against dip

crown could occur (Goodman 1989; Aydan *et al.* 1993; Diederichs and Kaiser 1999; Potvin and Hadjigeorgiou 2008). This failure mode is known as "Buckling." Ortlepp and Stacey (1994) suggested "Buckling" failure as one of the primary rock-burst mechanisms, in which rock slabs formed by parallel joints burst into the tunnel. From the observation at Big Bell Gold Mine, Sandy and Player (1999) showed "Buckling" at the sidewalls where thinly laminated tangential to the periphery of the tunnel. Bossart and Wermeille (2003), Marschall *et al.* (2006), Blümling *et al.* (2007), Labiouse and Vietor (2014), and Lisjak *et al.* (2015) investigated the "excavation damaged zone" (EDZ) surrounding the tunnel in Opalinus claystone at the Mont Terri Underground Rock Laboratory (URL). They revealed that the "Bending and Buckling" layers would occur at locations where layers were parallel to the tunnel periphery. Based on the experiences at Lapa and LaRonde mines, Mercier-Langevin and Wilson (2013) showed that the weak foliated rock was specifically sensitive to buckling failure owing to the stress redistribution around the excavation.

[1] Ph.D. candidate, Department of Civil Engineering, National Central University, Taoyuan City 32001, Taiwan.

[2*] Professor (corresponding author), Department of Civil Engineering, National Central University, Taoyuan City 32001, Taiwan (e-mail: ymt@cc.ncu.edu.tw).

[3] Professor, Department of Civil Engineering, National Central University, Taoyuan City 32001, Taiwan.

[4] Ph.D., Department of Civil Engineering, National Central University, Taoyuan City 32001, Taiwan.

Besides, Aydan *et al.* (1993) researched the squeezing potential of rock around the tunnel. They revealed that "shearing and sliding" failure could occur in thickly laminated sedimentary rocks. Marschall *et al.* (2006), Lisjak *et al.* (2015) showed the failure pattern of "sliding" along the bedding plane at the right sidewall of HG-A micro-tunnel at the Mont Terri URL when tunnel direction parallels the bedding strike.

In the case of excavation perpendicular to the strike of the joint or the bedding plane, Bossart *et al.* (2002), Bossart and Wermeille (2003), Bossart *et al.* (2004), Blümling *et al.* (2007), and Lisjak *et al.* (2015) found the EDZ around the tunnel in Opalinus claystone in the Mont Terri URL. The EDZ showed the unloading fractures parallel to the sidewall and shear fractures parallel to the bedding planes at the crown and invert. Nussbaum *et al.* (2011) found the new shear fractures sub-parallel to the tunnel face when the excavation direction was perpendicular to the bedding plane or fault. Fortsakis *et al.* (2012) studied the displacement and bending moment behaviors of stratified rock masses in tunneling. They found that the maximum displacement and bending moments were observed at the positions where the bedding planes or joints were tangential to the periphery of the tunnel.

With the advances of numerical models, many investigators began to study the failure mode or failure process of rock mass around the tunnel in the transversely isotropic rock mass. Jiang *et al.* (2006), and Jiang *et al.* (2009) investigated the cracking process near a large tunnel in a jointed rock mass (with one joint set) using UDEC and EDEM. They found that the most common failure types were "falling" from the crown and "sliding" from the sidewall with the joints dipping in the tunnel. Jia and Tang (2008), and Wang *et al.* (2012) investigated the failure modes around the tunnel in a transversely isotropic rock mass using a numerical code titled "Realistic Failure Process Analysis" (RFPA2D). Their study found that the dip angle of laminated layers had a crucial role in governing the cracking process around the tunnel.

More recently, the particle flow code (PFC) has become popular in numerical modeling due to its capability in modeling the micro-cracking process of the material. Taking advantage of the unique features of PFC, Sagong *et al.* (2011), Yang *et al.* (2016), Cao *et al.* (2018), Yang *et al.* (2019), and Lin *et al.* (2020) studied the failure characteristics of a circular hole in jointed specimens under uniaxial and biaxial compression. They found that the dip angle influenced the cracking process and failure pattern around the hole. Although many studies had been reported, knowledge about the failure evolution and failure characteristics around the tunnel in the transversely isotropic rock mass is still inadequate. The previous studies based on the observations from the tunnel projects captured only an incomplete relationship between the tunneling direction and the orientation of geological structures. Further, the vast majority of previous numerical studies focused on 2D modeling of the cracking evolution and failure pattern. The failure behavior was investigated with a circular hole tunnel model under uniaxial and biaxial compression loading. The limitations in these studies were noted.

In the present study, we investigate the failure modes around the tunnel under a three-dimensional stress state using PFC3D. Three scenarios regarding to relationships between tunneling direction and joint orientation (dip and dip direction of joints), as shown in Fig. 1, are analyzed. In each scenario, the tunneling process is divided into several steps to secure the most relevant results.

In the following sections, Section 2 presents the methodology and numerical experimentation details; Section 3 discusses the results of the numerical experimentation and the implications of the presented results; and finally, Section 4 summarizes the findings and presents the concluding remarks.

2. METHODOLOGY AND DETAILS OF NUMERICAL MODELING

2.1 Synthetic Rock Mass Model

The synthetic rock mass is a conceptual model to simulate the behavior of jointed rock mass in numerical simulation. It is created by combining the intact rock and joint sets from the Discrete Fracture Network (DFN) model.

Intact rock is like an entire block among discontinuities. In the present study, the intact rock is created by adopting the bonded-particle model (BPM) (Potyondy and Cundall 2004). The bonded-particle model is a conceptual assembly of spherical particles glued at their contact points. The breakage can only occur at the contact point when the applied force exceeds the bond strength of the contact point. Herein, the mechanical behavior of contact points between particles is simulated by a linear parallel bond model representing the mechanical response of finite-sized pieces jointed by a cement material (Itasca 2014). Due to the bond between particles based on the finite-sized pieces, both force and moment can be transmitted (Itasca 2014). The linear parallel bond model has already been confirmed to be appropriate to simulate the rock-like material (Sagong *et al.* 2011; Yang *et al.* 2016; Cao *et al.* 2018; Yang *et al.* 2019; Lin *et al.* 2020). Here, this contact model is usually applied to generate the intact rock model.

As an example, the intact rock model simulates the behavior of the fine-grained sandstone. The mechanical properties and the stress-strain curve of fine-grained sandstone under the uniaxial compression are shown in Fig. 2. The calibration process is carried out to determine the micro-parameters of the linear parallel bonded model so that the simulation matches the experiment. Based on the calibration process proposed by Yoon (2007), Ma and Huang (2018), the trial-and-error approach was carried out. Figure 2 shows that the stress-strain curve of the PFC3D simulation fits 13 very well with the experimental results. The best micro-parameters of the linear parallel bonded model are listed in Table 1. The maximum and minimum particle radius ratio (R_{max}/R_{min}) is 1.5, in which the minimum particle radius is 0.133 m. The particle density (Δ) is 2,650 kg/cm^3. The porosity (ρ) of the intact rock model is set at target value of 0.2. These micro-parameters are used to create the intact rock model with the size of $30 \times 30 \times 30$ m^3.
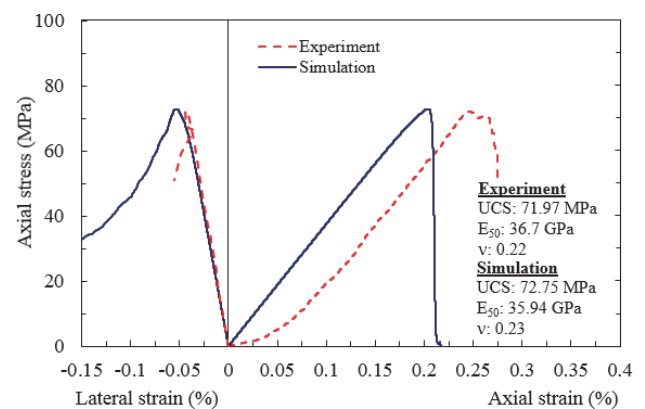

Fig. 2 Stress-strain curves of the laboratory test and PFC3D simulations

Table 1   Micro-parameters of the linear parallel bond model

Micro-mechanical parameters		Values
Linear micro-parameters	Contact modulus, E^* (GPa)	20.5
	Normal to shear stiffness ratio, k_n/k_s	3.0
	Friction coefficient, µ	0.50
Parallel-bond micro-parameters	Radius multiplier, λ	1.0
	Effective modulus, $\bar{E}^*$ (GPa)	20.5
	Normal to shear stiffness ratio, $\bar{k}_n/\bar{k}_s$	3.0
	Tensile strength, $\bar{\sigma}_c$ (MPa)	15.0
	Cohesion, $\bar{c}$ (MPa)	35.0

Table 2   Micro-mechanical parameters of the smooth-joint model

Micro-mechanical parameters	Values
Shear stiffness per unit area, sk_s (N/m/m²)	1.05×10^9
Normal stiffness per unit area, sk_n (N/m/m²)	5.63×10^9
Joint friction coefficient, µ	0.50
Joint cohesion, c	0.0
Joint tensile strength, σ_c (MPa)	0.0
Large strain (−)	1

The micro-parameters of the smooth joint model are shown in Table 2. Figure 3 illustrates the results of direct shear simulations. The friction angle and cohesion of joint are 39.25° and 1.76 MPa, respectively.

The joint set is represented by the DFN model, a conjectural model expressing geometrical relations between fracture sets and fractures and the geometrical properties of each fracture (Lei *et al.* 2017). The DFN model is generated from the commercial software FracMan (Golder Associates. 2011). The DFN model involves an assembly of fractures. It is generated based on the geometrical parameters, including fracture intensity (P32), fracture orientation (*i.e.,* dip direction and distribution of joint dip direction), and fracture size. In the present study, the DFN model only contains one joint set. The DFN model with the size of 30 m × 30 m × 30 m is generated with a set of geometrical parameters involving the equivalent fracture diameter of 5 m and fracture intensity (P32) of 1 m²/m³. The Fisher distribution represents the dip direction of the joints. In this model, all joints are identically parallel to each other, and the Fisher constant, an essential parameter of Fisher distribution, is set up as an infinity. Seven dip angles (*i.e.,* 0°, 15°, 30°, 45°, 60°, 75°, and 90°) are created and adopted for analyses. The mean of a joint spacing is roughly 1.0 m.

After the DFN model is generated, it is embedded into the intact rock model to form the synthetic rock mass. The mechanical behavior of the joints in the synthetic rock mass is represented by the smooth-joint model that reproduces the behavior of a planar interface. All contacts lying on the opposite sides of the joints are assigned by the smooth-joint model. The mechanical behavior of the planar interface is linearly elastic and frictional.
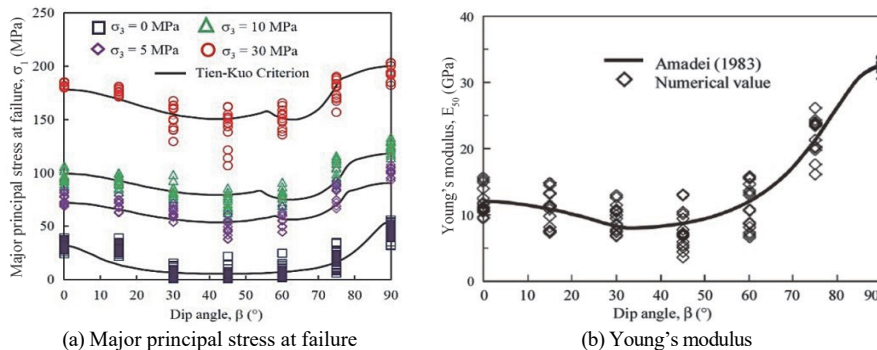
The macroscopic behavior of the synthetic rock mass is governed by the behavior of both the linear parallel bond model and the smooth-joint model. The model size of the synthetic rock mass in this study is 30 m × 30 m × 30 m. Seven models of the synthetic rock mass are generated corresponding to seven joint dip angles mentioned previously. The synthetic rock mass is generated with a large number of particles (*i.e.,* 230,652 particles). The accuracy of the model can be enhanced by further refining these particles. However, if the diameter of the particles is getting too small, the computational effort will be unbearable.

To properly investigate its elastic and strength behavior, we randomly selected 15 samples (with a size of 3 m × 3 m × 6 m) for each joint dip angle from the synthetic rock mass. The uniaxial and triaxial compressive tests are carried out, in which the triaxial compressive test is conducted with three levels of confining pressures (5, 10, and 30 MPa). The strength and Young's modulus corresponding to the dip angles of the joints are presented in Fig. 4. The results show the anisotropic behaviors of the synthetic rock mass under different joint dip angles. The Tien-Kuo criterion (Tien and Kuo 2001) for transversely isotropic rock mass is adopted to delineate the strength anisotropy of the synthetic rock mass. It is noted that the synthetic rock mass behaves like the transversely isotropic rock mass.

(a) Numerical results of shear displacement and shear stress   (b) Frictional feature of the joint
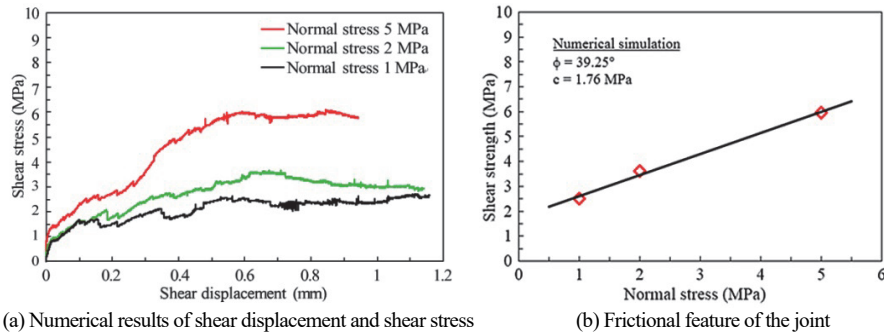
Fig. 3   Numerical direct shear test

(a) Major principal stress at failure   (b) Young's modulus

Fig 4   Anisotropic mechanical properties of synthetic rock mass (Amadei 1983)

2.2   Tunneling Excavation Procedure

After the synthetic rock mass models for seven joint dip angles are generated, the three-dimensional stresses are applied (σ_1 = 50 MPa, $\sigma_2 = \sigma_3$ = 10 MPa), as shown in Fig. 5. The major principal stress (σ_1) is the vertical stress, whereas the intermediate and minor principal stresses (σ_2, σ_3) are the lateral stresses in which the direction of σ_2 parallels the tunnel axis. When σ_2 and σ_3 reach the target value of intermediate and minor principal stresses, they will be kept constant. The vertical stress continues increasing to the target value before it is remained unchanged, as illustrated in Fig. 5(a). When the principal stresses reach the target values, the bottom plane is set to zero displacements (x, y, and z displacements are set to zero). Two planes perpendicular to the tunnel axis are fixed at "plane strain" conditions. High σ_1 and low lateral stress ratio of 0.2 are adopted to ensure that failure can be observed in the excavation stage.

To simulate the effect of tunneling direction on tunnel stability in the face of joint orientation, we analyzed the three scenarios mentioned previously. In each scenario of tunneling direction relative to the joint orientation, seven different joint dip angles (*i.e.*, 0°, 15°, 30°, 45°, 60°, 75°, and 90°) are adopted in sequence in the analysis. The tunnel has a circular shape with a length of 15 m and a diameter of 5 m. The excavation process is divided into six steps. The excavation length of each step is about 2.5 m, as illustrated in Fig. 6. The construction procedure of full-face excavation without the support of any reinforced system is assumed. In each excavation step, the balls lying on the extent of each step are deleted simultaneously. A certain number of calculation cycles are set up so that the state of the model reaches an approximate equilibrium before the next step is carried out. In this study, the model size (boundary) is six times larger than the tunnel diameter, which is considered adequate for numerical analysis.

A measurement system consisting of displacement and stress gauges is installed to record the stress and displacement around the tunnel, as presented in Fig. 6. This measurement system is established along the tunnel axis and at a cross-section 10 m from the tunnel face. The gauges are arranged with a space of 2.0 m. These gauges are set far from the tunnel boundary (at least 1.0 m) to eliminate the local failure on the tunnel boundary. As the synthetic rock mass, which contains many joints, is a heterogeneous medium, the stresses around the tunnel show considerable variation. This study uses the degree of stress change (δ) to represent the stress change around the tunnel caused by excavation. The degree of stress change is defined as the ratio of stress change over the initial stress:
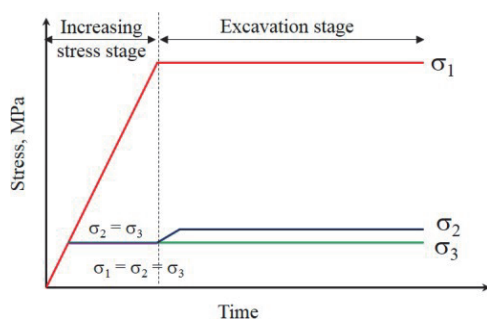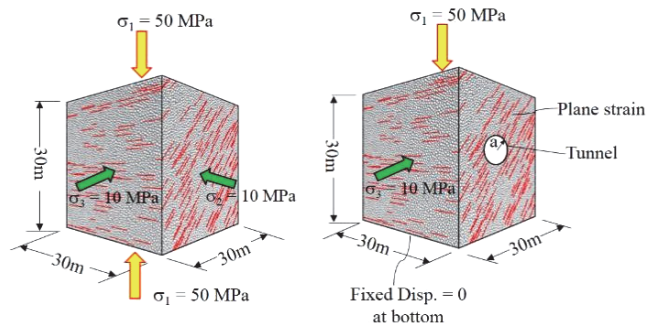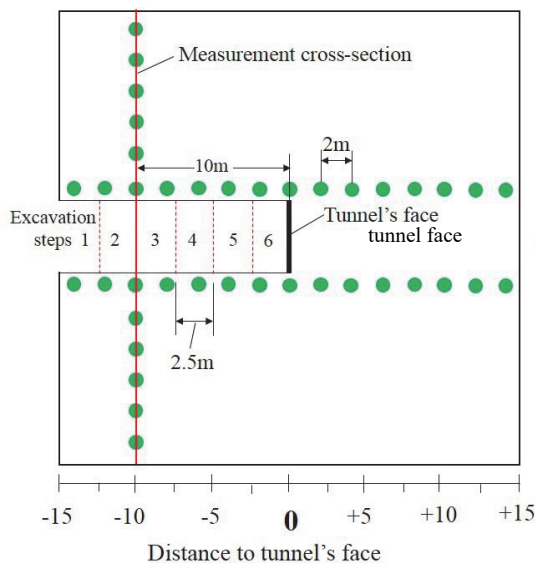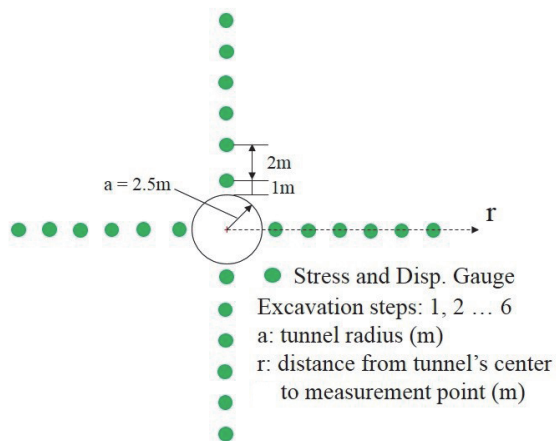

(a) Stress path   (b) Boundary conditions before and during excavation

Fig. 5   Stress state before and during excavation

(a) Along the tunnel   (b) Perpendicular to the tunnel axis

Fig. 6   Measurement system for displacement and stress (cross-section measurements)

$$\delta = \frac{\sigma_f - \sigma_i}{\sigma_i} \qquad (1)$$

where σ_i = the initial stress, and σ_f = the stress after excavation.

3.1   Displacement Field Around the Tunnel

The characteristics of stress and displacement are clear signs to identify the damage. In PFC, the displacement magnitude and the displacement direction of particles provide the further understanding of the damage process and damage state. It was popularly used to investigate the cracking process and failure in numerical model (Zhang and Wong 2014, Yang *et al.* 2019, Lin *et al.* 2020). The characteristics of displacement magnitude and direction are presented by the displacement field, which is referred to as the distribution of displacement vectors of the particles in a domain. The displacement vectors of the particles would be displaced from one state to another due to the excavation (Zhang and Wong 2014). In the BPM, each displacement vector gives the magnitude and direction of the displacement of each particle. The displacement vector is described as a solid arrow arising from the particle's center. Here, a color scale from dark blue to red is used to express the displacement magnitude. The dark blue depicts the minimal displacement, whereas the red displays the maximal displacement (Fig. 7).

Figure 7 shows the displacement field at the measurement cross-section (as shown in Fig. 6) with a dip angle of 45° before and after excavation. In an initial state, all displacement vectors follow the same direction and their magnitudes are approximately the same, as shown in Fig. 7(a). Due to the tunnel excavation, the excavation-induced stress redistribution causes the displacement around the tunnel. The closer the vicinity of the tunnel periphery, the larger the displacement. This results in the fact that the displacement field changes abruptly in the vicinity of the tunnel during the excavation, as shown in Fig. The abrupt change of the displacement direction and magnitude in the proximity of the inherent joint around the tunnel shows the cracking processes and the movement of rock blocks.

Because the inherent joints have a crucial role in the displacement, stress concentration, and failure around the tunnel, the displacement fields are considered based on the cracking processes and the tendency of the rock block to lie on opposite sides of the inherent joints. Four types of displacement fields are classified based on the cracking processes and the movement of particles surrounding the tunnel. They are tensile displacement

around the joint (DF-I), tensile displacement in 13 an intact rock (DF-II), shear and tensile displacement (DF-III), and shear displacement (DF-IV), as shown in Fig. 8. In the displacement field, the displacement magnitude of particle sets is analyzed to interpret the damage tendency, as indicated in Fig. 8. The displacement vectors of the corresponding particle sets are depicted by the red and blue arrows. The red arrow shows a larger displacement than the blue arrow does. The direction of arrows indicates the displacement direction of the particle set. S_a and S_b represent the displacement magnitude of two particle sets corresponding to the blue arrow and the red arrow, respectively. The category of the displacement fields provides the further understanding of damage process and damage states (tensile, shear or both tensile and shear).

The tensile displacement type (DF-I) is delineated by particle sets lying on the opposite sides of the joints, in which the displacement magnitude of one particle set is much greater than that of the other ($S_a \ll S_b$). In this type, the trend line having a larger displacement magnitude (S_b) moves 'normal' to (*i.e.,* in a direction perpendicular to) the joint surface; the other (S_a) can move normal to or along the joint surface. Because the predominance of the particle set is normal to the joint, it causes the detachment of the particle set from the joint. The DF-I causes the separation of one particle set from another at the interface of the joint. Yang *et al.* (2019) and Lin *et al.* (2020) showed similar results.

In the case of the tensile displacement type in the intact rock (DF-II), the two particle-sets diverge from each other, in which one particle set has a much greater displacement than the other ($S_a \ll S_b$). The macro-tensile cracks are observed on the interface of the two particle-sets. The tensile displacement type (DF-II) occurs in the intact rock medium regardless of the inherent joints. It was also reported in the previous studies (Yang *et al.* 2019; Lin *et al.* 2020; Zhang and Wong 2014).

Fig. 8   Four displacement field types: (a) tensile displacement (DF-I); (b) tensile displacement in intact rock (DF-II); (c) shear and tensile displacement (DF-III); (d) shear displacement along the joint (DF-IV)
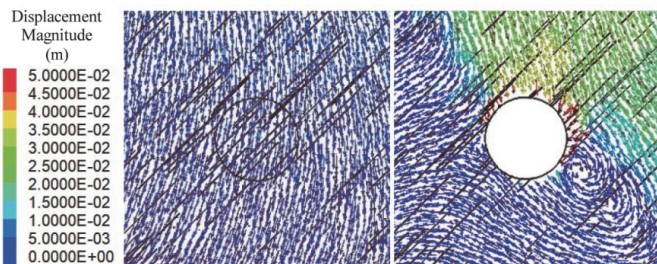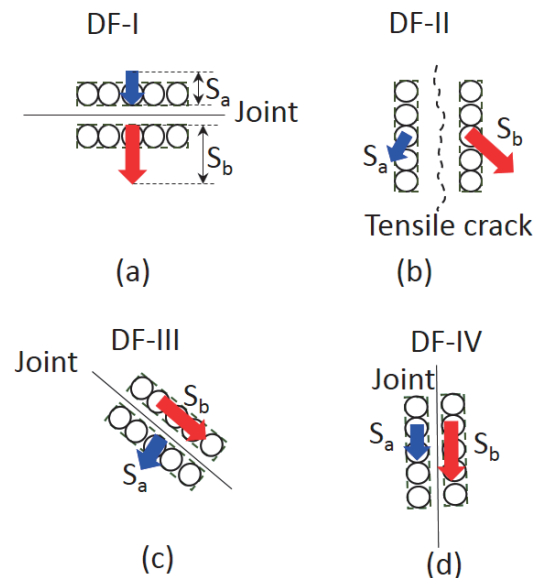

Fig. 7   Displacement field during excavation process at the measurement cross-section with a dip angle of 45° in Scenario I: (a) before excavation; (b) after excavation

The shear and tensile displacement type (DF-III) displays two displacement particle sets lying on opposite sides of the joint. The displacement of the particle set (S_b) moving tangent to the joint surface is larger than that of the other (S_a) moving normal to the joint surface. So, slipping and splitting co-exist in this type. This results in the coexistence of shear and tensile displacements on the joint surface between these particle sets. Because S_b is usually larger than S_a, the shear displacement along the joint is prominent. This type of displacement field is consistent with the previous report (Yang *et al.* 2019).

The shear displacement type (DF-IV) is described by two particle-sets lying on opposite sides of the joint, in which they move along the inherent joint in the same direction. The displacement of one particle set is larger than that of the other ($S_a <$ S_b). This type of displacement causes a relative shear displacement along with the interface of the joint.

Figure 9 illustrates the displacement fields around the tunnel with different dip angles in Scenario 1. In the case of low dip angles (*i.e.,* 0° ~ 30°), DF-I and DF-II are observed around the tunnel. Because of the effect of the excavation, the regions in the crown and invert of the tunnel are unloaded. The rock layers formed by the parallel joints in these regions tend to move into the tunnel. The layer close to the tunnel periphery displaces more than other layers. Thus, the DF-I is observed in the crown and invert of the tunnel, where the rock layers are tangent to the tunnel periphery. The DF-II occurs in the shoulder, left and right sidewalls with dip angles of 0° ~ 15°, the left shoulder with dip angle of 30°. When the rock layers formed by the separation of the joints are cut during the excavation, the overhanging end of the layers at the shoulder is bent. The DF-II is observed at this location.

In the case of dip angles ranging from 45° to 75°, the DF-I is seen in the left shoulder of the tunnel, where the joints are tangent to the periphery of the tunnel. In the right sidewall, where the joints dip in the tunnel, the rock mass lying on the joint surface moves along the joint into the tunnel, while the rock mass under the joints tends to move perpendicular to the joint. Thus, the DF-III is observed. In the case of vertical joints (i.e., β = 90°),

the DF-I is seen in the sidewalls, while the DF-IV is observed at the crown. At the crown, the rock layers tend to move along the joints.

Figure 10 presents the displacement field around the tunnel in Scenarios 2 and 3. At the crown and invert of the tunnel, the displacement fields in Scenarios 2 and 3 are similar. The trend line of the particle set close to the tunnel periphery tends to move perpendicular to the joints. At the same time, the other displaces in the vertical direction under the gravity or heaving force. The DF-I is observed at the crown and invert. At the sidewall, the trend line of the particle joint set near the tunnel wall tends to detach from the original position and move into the tunnel. The DF-II is the main feature of the displacement field in the sidewalls.
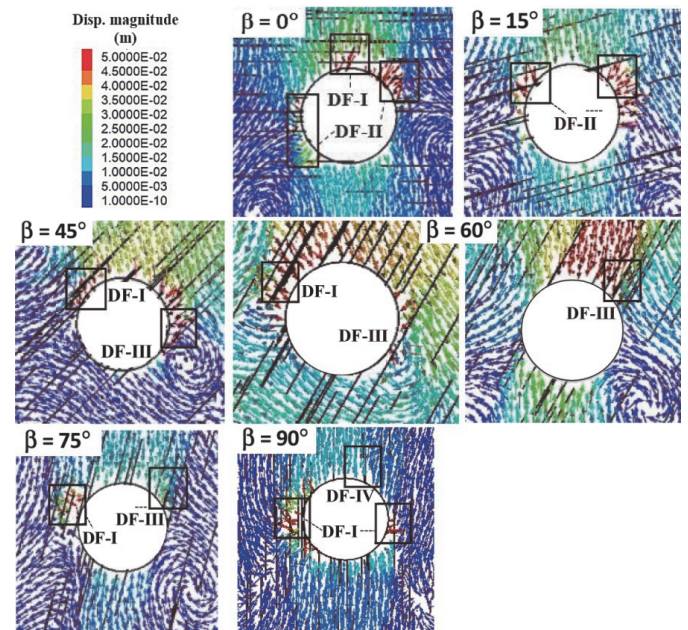

Fig. 9   Displacement fields of Scenario I
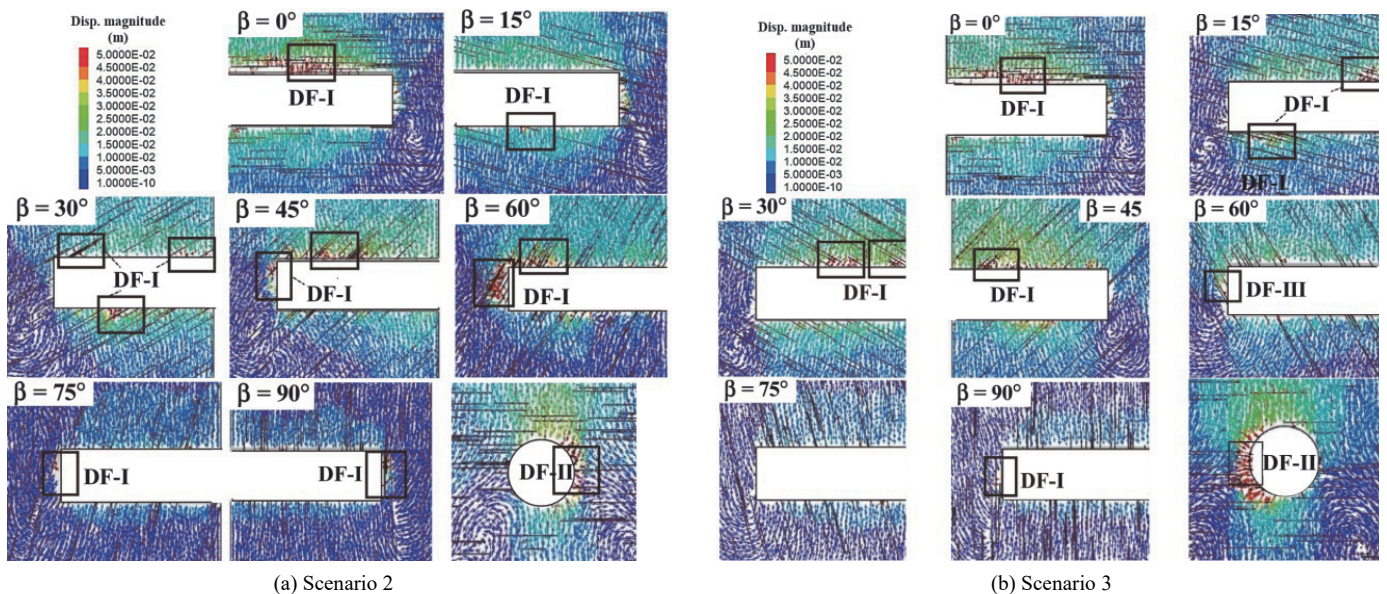

(a) Scenario 2

(b) Scenario 3

Fig. 10   Displacement fields

In the tunnel face, the displacement field shows the discrepancy between Scenario 2 and Scenario 3. In Scenario 2, with dip angles of 45°, 60°, and 75°, the rock layers detach from the initial positions. The displacement vectors are perpendicular to the joints. The DF-I represents the movement tendency of rock mass in this case. In Scenario 3, the displacement vectors of the rock layer with dip angles of 45° ~ 60° tend to move along the joint into the tunnel. The DF-III is observed in this case. With the vertical joints, the DF-I is the main feature of the displacement field in the tunnel face.

3.2 Tunneling Direction Parallel to the Joint Strike

As previously mentioned, our study covers seven different dip angles, including 0°, 15°, 30°, 45°, 60°, 75°, and 90°. The dip angle has a significant role in governing the displacement around the tunnel. The distribution of the 9 displacement and the force around the tunnel with different dip angles is shown in Figs. 11 and 12, respectively. With low dip angles (*i.e.,* 0° ~ 15°), the displacements distribute symmetrically at the crown. The extent of the displacement zone reaches two to three tunnel radii. The force completely decreases within a tunnel radius at the crown. The high force distributes at the sidewalls of the tunnel. The serious decrease in the force at positions occurring the larger displacement is observed, as shown in Fig. 12. The unloading zone has a tendency of rotating perpendicular to the joints. The failure is observed at the crown, shoulder, and sidewalls. The new cracks distribute relatively symmetrically around the tunnel. The extent of crack distribution is approximately at two times tunnel radius. Almost micro-cracks are oriented nearly parallel to the tunnel side wall with very high dip angle, as shown in Fig. 13.
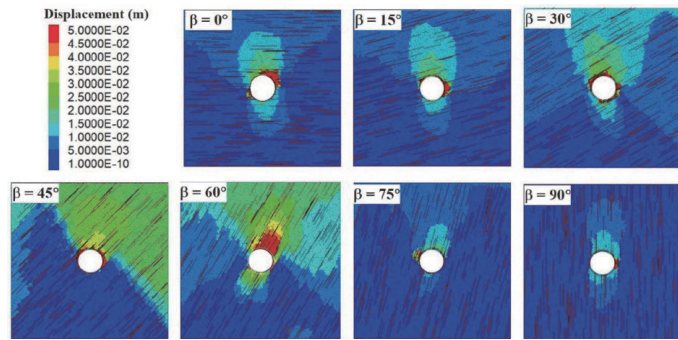

Fig. 11 Excavation induced displacement distribution at the measurement cross-section of Scenario 1
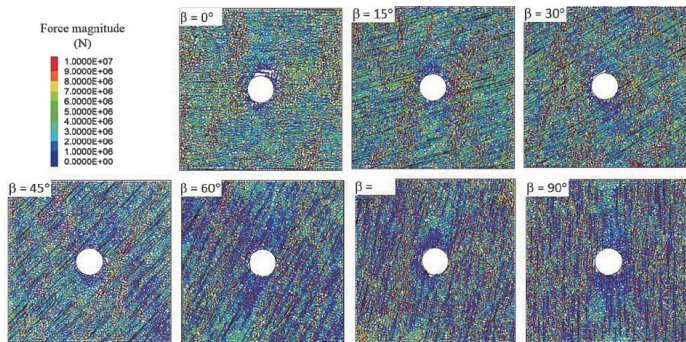

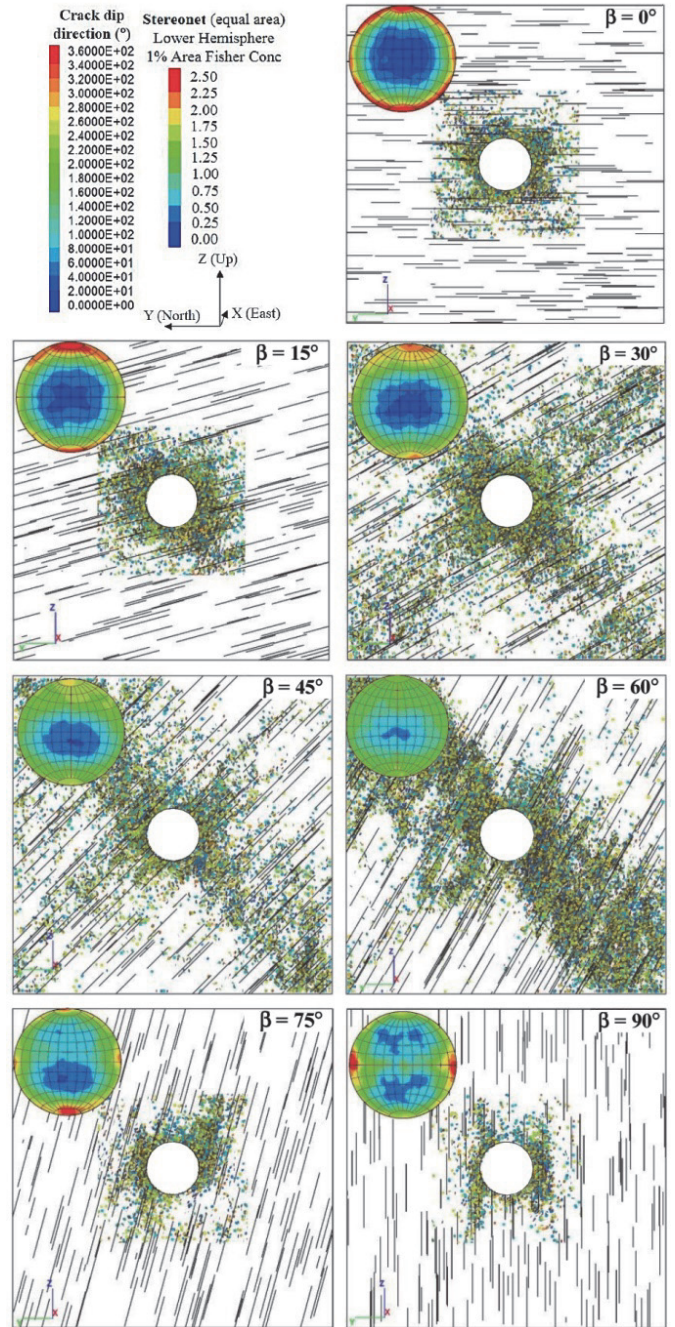**Fig. 12 Distribution of force chain at the measurement cross-section of Scenario 1**

Fig. 13 Crack distribution around the tunnel of Scenario 1

For medium dip angles of 30° ~ 60°, the extent of the displacement around the tunnel is the largest. Especially, the severe displacement is observed with the dip angles of 45° ~ 60°, as illustrated in Fig. 11. With dip angle of 30°, the force distribution is roughly similar to that of small dip angles. The unloading zone tends to rotate perpendicular to the joint. With dip angles of 45° ~ 60°, the force distributes along the joint. The unloading zone around the tunnel is governed by the joints, as shown in Fig. 12. Otherwise, the decrease in the force is observed in the direction perpendicular to the joint. The new cracks develop extensively and extend very far away from the tunnel boundary. With the dip angles of 30° ~ 45°, the new cracks develop in two directions. One is parallel to the joints, and the other is perpendicular to the joints. However, the cracks formed perpendicular to the joints in

the proximity of the tunnel have an essential role in causing the failure mode at the right shoulder of the tunnel. With a dip angle of 60°, the new cracks develop perpendicular to the joints. There is a transition in developing new cracks from two directions to one direction along the joint in medium dip angles. The shear cracks account for a considerable amount of total new cracks.

With high dip angles (*i.e.,* 75° ~ 90°), both the displacement magnitude and the extent of the displacement around the tunnel are minimal. However, the extent of the decrease in the force at the crown and invert expends relatively far from tunnel periphery. At the failure positions in the sidewall, the force decreases roughly to zero. The extent of the displacement and force is strongly governed by the joints, as illustrated in Figs. 11 and 12. The new cracks develop almost exclusively along the joint near the tunnel, as shown in Fig. 13.

Based on the stress, displacement, and crack evolution around the tunnel, the failures are identified. From the crack distribution and the failure around the tunnel, we classify the failures into four modes: Detaching and Buckling, Sliding, Bending and Spalling, and Slabbing and Spalling, as shown in Table 3. These failure modes are further described in the following.

(1) Detaching and Buckling mode

This mechanism may be explained by the excavation-induced stress redistribution leading to an increase in the loading and the dilation normal to the bedding planes at the sidewall. The dilation reduces the critical buckling load. In this study, this mode is observed at all dip angles. The parallel joints cut the rock mass into layers. The thickness of the layers depends on the random generation 49 of the joints. At thin layers that are tangent to the tunnel, the detaching and buckling failure is observed.

The failure locations tend to move around the tunnel from the crown to the left sidewall, corresponding to the increase in the dip angle. The detaching and buckling failure mode is observed at the crown with the low dip angles of 0° ~ 15°. The failure position appears at the left shoulder with the dip angles of 30° ~ 60°, while it is observed at the Sid walls with high dip angles (*i.e.,* 75° ~ 90°). Otherwise, the detaching and buckling failure mode is seen at the bottom of the tunnel with dip angles of 0° ~ 30°. In the cases studied, the DF-I governs the detaching and buckling failure.

Table 3   Failure modes around the tunnel

Failure mode	Signs	Description
Detaching and Buckling		
Sliding		
Bending and Spalling		
Slabbing and Spalling		

(2) Sliding mode

This failure mode is observed at the right sidewall with dip angles of 45° ~ 60°. New cracks develop perpendicular to the joints, and they are merged to form the fractures. The intersection between the joints and fractures creates the rock blocks at the right sidewall. The rock blocks tend to slide along the joints into the tunnel. This failure mode causes the catastrophic failure of the tunnel. The displacement field type (DF-III) is observed in the vicinity of the right sidewall with dip angles of 45° ~ 60°. It is a characteristic of sliding failure along the joints with medium dip angles.

With high dip angles (β = 75° ~ 90°), although the sliding mode was not observed, the displacement field type (DF-III) at the right sidewall of the dip angle of 75°, DF-IV at the crown of the dip angle of 90° as well as the significant decrease in axial stress at the crown would be shown the potential risk of the sliding mode failure. Figure 14 shows the degree of axial stress change at the crown at the measurement cross-section. It showed that the decrease in axial stress with high dip angles (*i.e.,* 75° ~ 90°) extends very far from the tunnel periphery compared to that of other dip angles. This facilitates the rock mass sliding along the joints into the tunnel with the high dip angles.

(3) Bending and spalling mode

This failure mode occurs at the shoulder of the tunnel with a dip angle of 0° ~ 15° and at the left shoulder with 30° ~ 45° dip angles. The parallel joints separate the rock mass into layers (beams). Due to the tunnel excavation, one end of the layers on the tunnel periphery is free and missed the supporting pressure. It behaves like an overhanging beam. Under the excavation-induced stress concentration and the displacement distribution around the tunnel, the pressure and bending moment will act at the overhanging end, leading to the "bending and spalling" failure. In this failure mode, the DF-II is observed at the failure position of the overhanging beam, and the macro-tensile crack propagates perpendicular to the inherent joint. The maximum bending moments are the main cause of bending and spalling failure mode. 13 This mode is consistent with the investigation by Sagong *el al.* (2011).

(4) Slabbing and spalling mode

This failure mode is observed at the sidewalls with low dip angles (*i.e.,* 0° ~ 15°). The DF-II is the main characteristic of this failure mode. Under the high-stress concentration at the sidewalls, the micro-cracks distribute around the tunnel and are oriented nearly parallel to the

tunnel side wall as shown in Fig. 13. They are merged to form the macro-tensile cracks (extensional fractures) parallel to the tunnel side wall. The macro-tensile cracks can cut through the inherent joints. The extensional fractures cut the rock mass from the sidewall into the slabs. The slabs at the sidewalls are detached and spalled into the tunnel.

The dip angle has a vital role in controlling the failure mode based on the previous discussions. It is clear that with a dip angle in the range of 0° ~ 30°, the "detaching and buckling" and "bending and spalling" are dominant. On the other hand, the "slabbing and spalling" failure mode is seen popularly at the sidewall with dip angles of 0° ~ 15°. With dip angles of 45° ~ 60°, the sliding along the joint at the right sidewall is predominant, which often causes the severe failure of the tunnel. In addition, the "detaching and buckling" and "bending and spalling" are observed at the left sidewall where the rock layers tangential to the tunnel wall. The "detaching and buckling" mode is a feature of the failures at the sidewalls with high dip angles (β = 75° ~ 90°).

3.3 Tunnel Axis Perpendicular to Joint Strike-Tunneling with Dip

In Scenario 2, the tunnel is excavated perpendicular to the joint strike, and the joints dip into tunnel direction. Figure 15 shows the displacement distribution at cross-section along the tunnel axis with varying dip angles. With the dip angles of 0° ~ 60°, the displacement distributions are relatively similar. The displacement develops almost exclusively at the crown and the invert. The displacement distributes roughly symmetrically in the tunnel crown. The crack intensity around the tunnel remains about the same when the dip angle is in the range of 0° ~ 60°. The extent of crack development is about two times tunnel radius. Almost cracks are oriented nearly parallel to the tunnel wall with high dip angle, as illustrated in Fig. 16. The similar results was shown by Bossart *et al.* (2002).

With high dip angles (*i.e.,* 75° ~ 90°), the tunnel's displacement is much lower than that with lower dip angles. The cracks distribute almost exclusively at the sidewalls. The extent of crack distribution is approximately 0.5 tunnel radius. The cracks are approximately parallel to the tunnel side wall, as shown in Fig. 16.
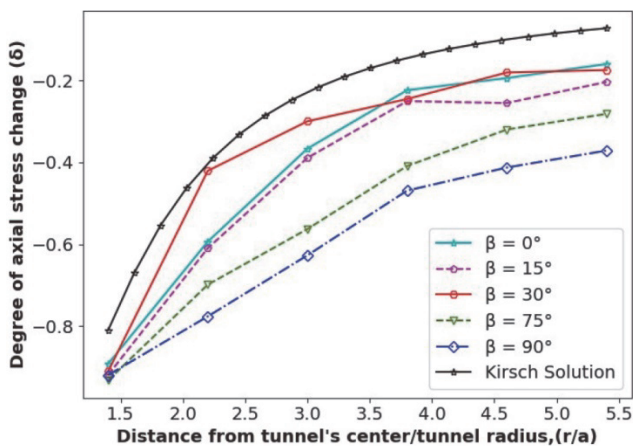

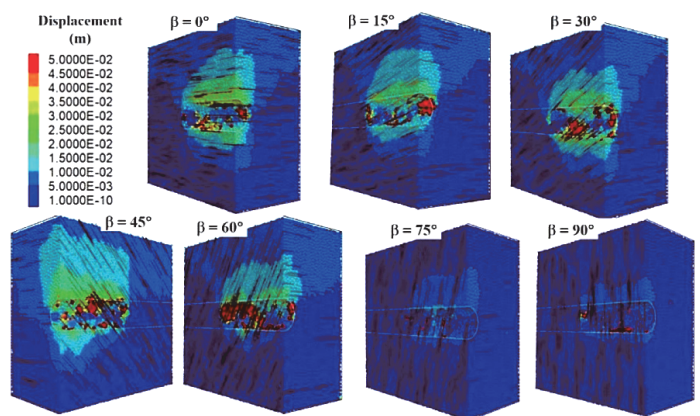**Fig. 14   Degree of axial stress change at the crown of the measurement cross-section**

Fig. 15   Displacement at cross-section along tunnel axis of Scenario 2
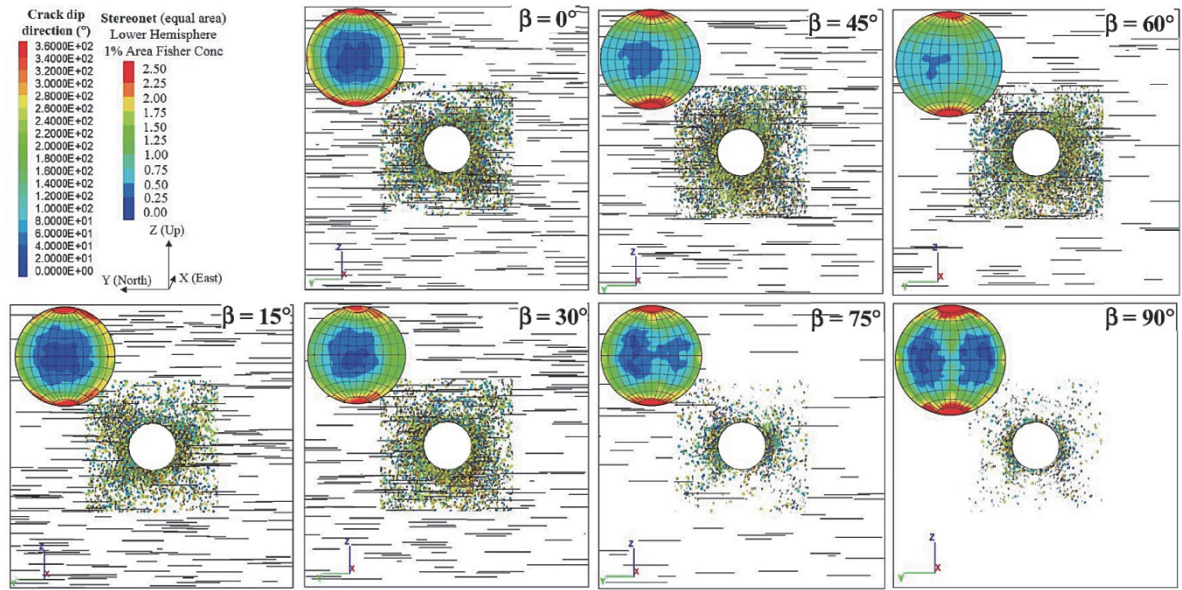
Fig. 16   Crack distribution around the tunnel of Scenario 2

The failures around the tunnel are analyzed. With low dip angles (*i.e.*, β = 0° ~ 15°), the failure modes are shown to be similar to that of Scenario 1. The "slabbing and spalling" mode is observed in the sidewall. The "bending and spalling" is seen in the shoulder. With high dip angles (*i.e.*, β = 75° ~ 90°), the tunnel is very stable. The local failure can be observed at the crown. This is the fall of the rock blocks at the crown of the tunnel. However, it is minimal and local. Some failure modes are classified based on the failures around the tunnel, as shown in Table 4.

Table 4   Failure modes in Scenario 2

Failure mode	Signs	Description
Bending and Spalling		
Slabbing and Spalling		
Falling		
Detaching and Buckling		

The failure modes in Scenario 2 are described in the following.

"Bending and spalling" mode is the failure characteristics in the crown with dip angles of 0° ~ 60° as shown in Figs. 10(a) and 15. The parallel joints cut the rock mass into thin layers. In view of the excavation-induced displacement, the closer to the tunnel periphery, the larger the displacement. Considering different displacements in the vicinity of the tunnel crown and invert, the end of rock layers cut by the tunnel excavation (overhanging beam) tends to experience the largest moments. In addition, the overhanging end of the layers tends to bend because of the sudden unloading, which often results in damage at the overhanging end, and the rock block falls into the tunnel's space. At the invert of the tunnel, this failure mode is often observed. However, the frequency and scale of the failure are less than those at the crown. The tensile displacement field type (DF-I) is the main characteristic of this mode. The movement direction of the damaged rock blocks is perpendicular to the joint, whereas the overall movement direction of rock mass follows the gravity direction. The damaged rock blocks tend to be bent and detached from the joints.

With high dip angles (*i.e.*, 75° ~ 90°), "Bending and spalling" failure is not observed at the crown and invert (Figs. 10(a) and 15). The reason is that the displacement direction of rock mass is nearly parallel to the joint. The bending moment acting at the free end of rock layers is small; it is not large enough to break rock layers.

"Slabbing and spalling" mode is observed at the sidewalls with dip angles of 0° ~ 60°. However, with high dip angles of 75° ~ 90°, the sidewalls are stable. Under the high-stress concentration, the rock mass is slabbed into layers. The layers or slabs are parallel to the tunnel wall and cut through the joints. The cracks develop extensively at the sidewalls and are oriented nearly parallel to the tunnel side wall, as shown in Fig. 16. The microcracks merge to form the fractures that are parallel to the tunnel wall. The rock mass in the sidewall is separated into slabs by fractures. From the perspective of the displacement field, the DF-II represents this failure mode, which is commonly seen in Scenario 2.

Falling mode is observed at the tunnel face when the joint dips into the tunnel direction. The joints separate the rock mass into the thin layers that dip into the tunnel direction. Under the high-stress concentration at the tunnel face, the thin layers near the tunnel face are spalled and felt into the tunnel space. The DF-I is observed in falling failure mode. This failure mode is commonly seen in cases with dip angles in the range of 45° ~ 75°. With the dip angles in the range of 0° ~ 30°, it is rarely observed.

"Detaching and Buckling" mode occurs at the tunnel face with a dip angle of 90°. The joints separate the rock mass into thin vertical layers. Under the high-stress concentration on the tunnel face, the thin layers are detached from the rock mass and spalled. The DF-I is observed in this failure mode.

The dip angle has a significant influence on the displacement distribution. However, the failure mode around the tunnel is similar with the dip angles in the range of 0° ~ 60°. In these dip angles, the bending and spalling of the layers at the crown and invert are observed. The lower the dip angle, the longer the overhanging end of the rock layer. Thus, the frequency of failure in lower dip angles is higher than that of high dip angles. The slabbing and spalling mode is prevalent at the sidewall. With dip angles of 75° ~ 90°, the bending and spalling mode is not observed. The failure sometimes occurs at the tunnel face with the "Detaching and Buckling" failure mode. However, the extent of the failure is negligible.

3.4 Tunnel Axis Perpendicular to Joint Strike-Tunneling Against the Dip

Scenario 3 simulates the tunnel excavation against the joint dip direction. Seven cases with different dip angles are considered in this series of analyses. The displacement distributes almost exclusively at the tunnel crown, as illustrated in Fig. 17. With a dip angle in the range of 0° ~ 45°, the extent of the displacement distribution increases. Especially, the displacement extends far from the tunnel boundary at dip angle of 45°. The cracks distribute mainly within two tunnel radius, and symmetrically around the tunnel, as shown in Fig. 18. The orientation of the cracks is roughly similar that of scenario 2, parallel to the tunnel sidewalls. The failures are observed at the crown, shoulder, sidewall, and tunnel face. However, they are most frequently seen in the crown and sidewall.

The extent of the displacement distribution reduces with the increase in the dip angle (from 60° to 90°). With dip angles in the range of 75° ~ 90°, the displacement magnitude and extent of displacement around the tunnel are minimal. The displacement develops mainly in the close vicinity of the crown and invert. The cracks only distribute near the sidewalls and are oriented roughly parallel to the tunnel wall, as shown in Fig. 18. The number of cracks is much less than that with other dip angles. The failure is only seen at the crown and tunnel face, but generally of local nature and negligible.

Based on the failures around the tunnel, we can classify them into four failure modes, as shown in Table 5.

Bending and spalling mode is observed at the crown with dip angles in the range of 0° ~ 60°. The joints separate the rock mass into rock layers. The tunnel excavation cuts through the rock layers and creates a free end of rock layers at the tunnel crown. The displacement at the crown develops extensively. The closer to the tunnel boundary, the larger the displacement. Under the unloading and the displacement of the rock layers at the crown, the free end of the rock layers is bent and spalled into the tunnel space. Often, this failure mode is seen at the tunnel's invert. However, the scale is relatively small. The displacement
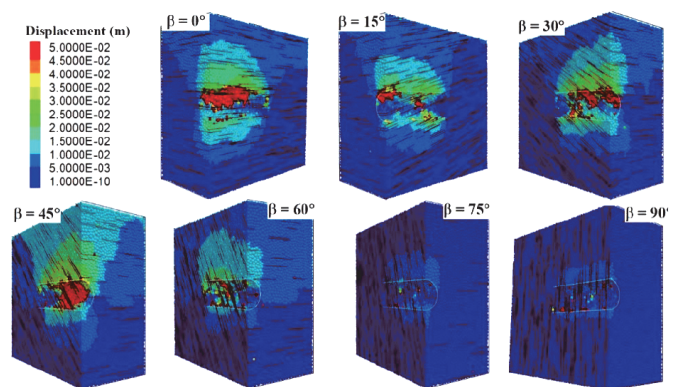

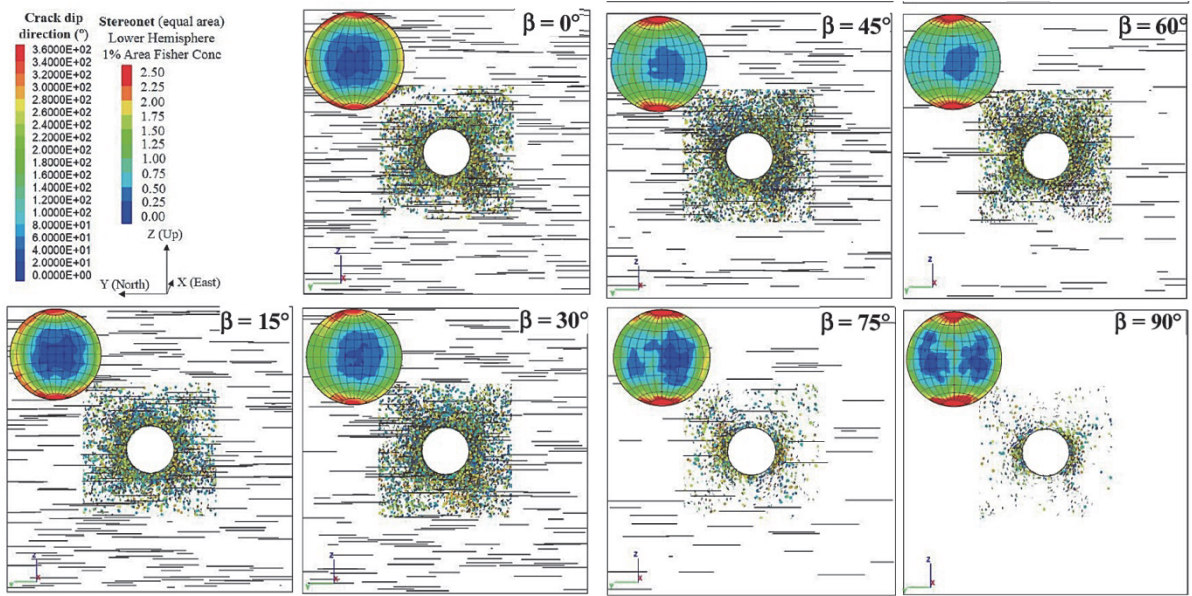**Fig. 17   The displacement at cross-section along tunnel axis of Scenario 3**

Fig. 18   Cracks distribution around the tunnel of Scenario 3

Table 5   Failure modes of Scenario 3

Failure mode	Signs	Description
Bending and spalling		
Slabbing and Spalling		
Sliding		
Detaching and Buckling		

trend line of the damaged rock block moves perpendicular to the joints. The DF-I is the main characteristic of this mode.

"Slabbing and spalling" mode occurs at the sidewall of the tunnel with the dip angles in the range of $0° \sim 60°$. Under the high-stress concentration at the sidewalls, the rock mass is slabbed into the thin layers parallel to the sidewalls by extensional fractures. The slabs can cut through the inherent joints. The extensional fractures are formed by merging the micro cracks that develop nearly parallel to the sidewall, as indicated in Fig. 18. The tensile displacement field in intact rock (DF-II) is the main characteristic of this mode.

"Sliding" mode is observed at the tunnel face, where the joints dip into the tunnel. It is only seen with the dip angles in the range of $45° \sim 60°$. The rock mass slides along the joints into the tunnel. It occurs most frequently at the upper part of the tunnel face. The DF-III the main characteristic of this mode.

At the tunnel face with vertical joints, the "Detaching and Buckling" mode is observed similar to the Scenario 2 as above represented.

In Scenario 3, the failure modes at the crown, invert, and sidewalls are similar to those in Scenario 2. With dip angles of $0° \sim 60°$, the "Bending and spalling" failure of thin layers is observed at the crown and invert, while "Slabbing and Spalling" failure mode is seen in the sidewall. At the tunnel face, the sliding failure mode is observed. The tunnel is stable with high dip angles (*i.e.,* $75° \sim 90°$). However, the "Detaching and Buckling" failure sometimes occurs at the tunnel face with a vertical joint dip angle.

4.   CONCLUSIONS

Tunneling in a transversely isotropic rock mass is always a challenging work due to the complicated variation of the in-situ stress, the geological medium, characteristics of joints as well as the relationship between excavation direction and joint orientation. It is difficult to cover all conditions. The obtained results in this study arise from the assumption of the transverse isotropy of the rock mass derived from one joint set. Three fundamental scenarios in different conditions of the joint dip angle were focused on to considered the failure modes and the characteristics of the displacement around the tunnel. The displacement field types and failure modes around the tunnel were classified to provide the further understanding of the damage process and damage state when excavation in the rock mass involving a single joint set. Four displacement field types were categorized: tensile displacement with the joint (DF-I), tensile displacement in intact 13 rock (DF-II), shear and tensile displacement field (DF-III), and shear displacement (DF-IV). The displacement field types help to figure out the origin of the crack type and the movement tendency of rock blocks in the close vicinity of the tunnel. DF-I represents the tearing around the inherent joints and existence of macro-tensile crack oriented perpendicular to the inherent joint. DF-II shows the development of extensional cracks or macro-tensile cracks around the tunnel. The DF-III and DF-IV show the tendency to the sliding movement of rock blocks along the inherent joints under different high dip angles.

The failure around the tunnel under each scenario was considered. In Scenario 1, four failure modes were found: "Detaching and Buckling," "Sliding," "Bending and Spalling," and "Slabbing and Spalling." The "Detaching and Buckling" mode

occurred at the locations where the joints were tangent to the tunnel wall. The "Sliding" mode was observed at the right sidewall with the dip angles of $45° \sim 60°$, where the joints dip into the tunnel wall. The "Bending and Spalling" mode was observed at the shoulder with dip angles of $0° \sim 15°$. The "Slabbing and Spalling" mode occurred at the sidewall with dip angles of $0° \sim 15°$.

In Scenarios 2 and 3, the failure modes around the tunnel were similar. The "Bending and Spalling" mode was observed at the crown. The "Slabbing and Spalling" mode occurred at the sidewalls, and the slabs formed by the coalescence of tensile cracks detached from the rock mass. The "Detaching and Buckling" mode was observed at the tunnel face with vertical joints. The difference between Scenario 2 and 3 was observed at the tunnel face with dip angles of $30° \sim 75°$. The "Falling" mode was shown in Scenario 2, whereas the sliding along the joint was observed in Scenario 3.

DATA AVAILABILITY

The data and/or computer codes used/generated in this study are available from the corresponding author on reasonable request.

CONFLICT OF INTEREST STATEMENT

The authors declare that there is no conflict of interest.

REFERENCES

1. Amadei, B. (1983). *Influence of Rock Anisotropy on Stress Measurements by Overcoring Techniques, Rock Anisotropy and the Theory of Stress Measurements*, Springer, Berlin, Heidelberg, 189-241.

2. Aydan, Ö., Akagi, T., and Kawamoto, T. (1993). "The squeezing potential of rocks around tunnels: Theory and prediction." *Rock Mechanics and Rock Engineering*, **26**(2), 137-163. https://doi.org/10.1007/BF0103265

3. Blümling, P., Bernier, F., Lebon, P., and Martin, C.D. (2007). "The excavation damaged zone in clay formations time-dependent behaviour and influence on performance assessment." *Physics and Chemistry of the Earth*, Parts A/B/C, **32**(8-14), 588-599. https://doi.org/10.1016/j.pce.2006.04.034

4. Bossart, P., Meier, P.M., Moeri, A., Trick, T., and Mayor, J.-C. (2002). "Geological and hydraulic characterisation of the excavation disturbed zone in the Opalinus Clay of the Mont Terri Rock Laboratory." *Engineering Geology*, **66**(1-2), 19-38. https://doi.org/10.1016/S0013-7952(01)00140-5

5. Bossart, P., Trick, T., Meier, P.M., and Mayor, J.-C. (2004). "Structural and hydrogeological characterisation of the excavation-disturbed zone in the Opalinus Clay (Mont Terri

Project, Switzerland)." *Applied Clay Science*, **26**(1-4), 429-448. https://doi.org/10.1016/j.clay.2003.12.018

6. Bossart, P. and Wermeille, S. (2003). *The Stress Field in the Mont Terri Region Data Compilation*, Reports of the Federal Office for Water and Geology, 65-92.

7. Cao, R., Cao, P., Lin, H., Ma, G., Fan, X., and Xiong, X. (2018). "Mechanical behavior of an opening in a jointed rock-like specimen under uniaxial loading: Experimental studies and particle mechanics approach." *Archives of Civil and Mechanical Engineering*, **18**, 198-214. https://doi.org/10.1016/j.acme.2017.06.010

8. Diederichs, M. and Kaiser, P. (1999). "Stability of large excavations in laminated hard rock masses: The voussoir analogue revisited." *International Journal of Rock Mechanics and Mining Sciences*, **36**(1), 97-117. https://doi.org/10.1016/S0148-9062(98)00180-6

9. Fortsakis, P., Nikas, K., Marinos, V., and Marinos, P. (2012). "Anisotropic behaviour of stratified rock masses in tunnelling." *Engineering Geology*, **141**, 74-83. https://doi.org/10.1016/j.enggeo.2012.05.001

10. Goodman, R.E. (1989). *Introduction to Rock Mechanics*, Vol. 2, Wiley, New York.

11. Itasca Consulting Group Inc., (2014). *Particle Flow Code in 3 Dimensions (PFC3D)*, Version 5.0, ICG, Minneapolis, MN.

12. Jia, P. and Tang, C. (2008). "Numerical study on failure mechanism of tunnel in jointed rock mass." *Tunnelling and Underground Space Technology*, **23**(5), 500-507. https://doi.org/10.1016/j.tust.2007.09.001

13. Jiang, Y., Li, B., and Yamashita, Y. (2009). "Simulation of cracking near a large underground cavern in a discontinuous rock mass using the expanded distinct element method." *International Journal of Rock Mechanics and Mining Sciences*, **46**(1), 97-106. https://doi.org/10.1016/j.ijrmms.2008.05.004

14. Jiang, Y., Tanabashi, Y., Li, B., and Xiao, J. (2006). "Influence of geometrical distribution of rock joints on deformational behavior of underground opening." *Tunnelling and Underground Space Technology*, **21**(5), 485-491. https://doi.org/10.1016/j.tust.2005.10.004

15. Labiouse, V. and Vietor, T. (2014). "Laboratory and in situ simulation tests of the excavation damaged zone around galleries in Opalinus Clay." *Rock Mechanics and Rock Engineering*, **47**(1), 57-70. http://dx.doi.org/10.1007/s00603-013-0389-4

16. Lei, Q., Latham, J.-P., and Tsang, C.-F. (2017). "The use of discrete fracture networks for modelling coupled geomechanical and hydrological behaviour of fractured rocks." *Computers and Geotechnics*, **85**, 151-176. https://doi.org/10.1016/j.compgeo.2016.12.024

17. Lin, Q., Cao, P., Meng, J., Cao, R., and Zhao, Z. (2020). "Strength and failure characteristics of jointed rock mass with double circular holes under uniaxial compression: Insights from discrete element method modelling." *Theoretical and Applied Fracture Mechanics*, **109**, 102692. https://doi.org/10.1016/j.tafmec.2020.102692

18. Lisjak, A., Garitte, B., Grasselli, G., Müller, H., and Vietor, T. (2015). "The excavation of a circular tunnel in a bedded argillaceous rock (Opalinus Clay): Short-term rock mass response and FDEM numerical analysis." *Tunnelling and Underground Space Technology*, **45**, 227-248. https://doi.org/10.1016/j.tust.2014.09.014

19. Ma, Y. and Huang, H. (2018). "A displacement-softening contact model for discrete element modeling of quasi-brittle materials." *International Journal of Rock Mechanics and Mining Sciences*, **104**, 9-19.

20. Marschall, P., Distinguin, M., Shao, H., Bossart, P., Enachescu, C., and Trick, T. (2006). "Creation and evolution of damage zones around a microtunnel in a claystone formation of the Swiss Jura Mountains." Paper presented at the *SPE International Symposium and Exhibition on Formation Damage Control*, OnePetro.

21. Mercier-Langevin, F. and Wilson, D. (2013). "Lapa mine — ground control practices in extreme squeezing ground." *Proc., Seventh International Symposium on Ground Support in Mining and Underground Construction*, Australian Centre for Geomechanics, 119-131.

22. Nussbaum, C., Bossart, P., Amann, F., and Aubourg, C. (2011). "Analysis of tectonic structures and excavation induced fractures in the Opalinus Clay, Mont Terri underground rock laboratory (Switzerland)." *Swiss Journal of Geosciences*, **104**(2), 187.

23. Ortlepp, W. and Stacey, T. (1994). "Rockburst mechanisms in tunnels and shafts." *Tunnelling and Underground Space Technology*, **9**(1), 59-65.

24. Potvin, Y. and Hadjigeorgiou, J. (2008). "Ground support strategies to control large deformations in mining excavations." *Journal of the Southern African Institute of Mining and Metallurgy*, **108**(7), 397-404.

25. Potyondy, D.O. and Cundall, P. (2004). "A bonded-particle model for rock." *International Journal of Rock Mechanics and Mining Sciences*, **41**(8), 1329-1364. https://doi.org/10.1016/j.ijrmms.2004.09.011

26. Sagong, M., Park, D., Yoo, J., and Lee, J.S. (2011). "Experimental and numerical analyses of an opening in a jointed rock mass under biaxial compression." *International Journal of Rock Mechanics and Mining Sciences*, **48**(7), 1055-1067. https://doi.org/10.1016/j.ijrmms.2011.09.001

27. Sandy, M. and Player, J. (1999). "Reinforcement design investigations at Big Bell." *Rock Support and Reinforcement Practice in Mining*, **301**.

28. Tien, Y.M. and Kuo, M.C. (2001). "A failure criterion for transversely isotropic rocks." *International Journal of Rock Mechanics and Mining Sciences*, **38**(3), 399-412. https://doi.org/10.1016/S1365-1609(01)00007-7

29. Wang, S., Sloan, S., Tang, C., and Zhu, W. (2012). "Numerical simulation of the failure mechanism of circular tunnels in transversely isotropic rock masses." *Tunnelling and Underground Space Technology*, **32**, 231-244. https://doi.org/10.1016/j.tust.2012.07.003

30. Yang, S.-Q., Yin, P.-F., Zhang, Y.-C., Chen, M., Zhou, X.-P., Jing, H.-W., and Zhang, Q.-Y. (2019). "Failure behavior and crack evolution mechanism of a non-persistent jointed rock mass containing a circular hole." *International Journal of Rock Mechanics and Mining Sciences*, **114**, 101-121. https://doi.org/10.1016/j.ijrmms.2018.12.017

31. Yang, X., Jing, H., and Chen, K. (2016). "Numerical simulations of failure behavior around a circular opening in a non-persistently jointed rock mass under biaxial compression." *International Journal of Mining Science and Technology*, **26**(4), 729-738. https://doi.org/10.1016/j.ijmst.2016.05.027

32. Yoon, J. (2007). "Application of experimental design and optimization to PFC model calibration in uniaxial compression simulation." *International Journal of Rock Mechanics and Mining Sciences*, **44**(6), 871-889.

33. Zhang, X.-P. and Wong, L.N.Y. (2014). "Displacement field analysis for cracking processes in bonded-particle model." *Bulletin of Engineering Geology and the Environment*, **73**(1), 13-21. https://doi.org/10.1007/s10064-013-0496-1